





Article

# Binder Jetting Additive Manufacturing: Powder Packing in Shell Printing

Guanxiong Miao <sup>1</sup>, Mohammadamin Moghadasi <sup>2</sup>, Ming Li <sup>3</sup>, Zhijian Pei <sup>3</sup>  and Chao Ma <sup>1,2,3,4,\*</sup> 

<sup>1</sup> Department of Mechanical Engineering, Texas A&M University, College Station, TX 77843, USA

<sup>2</sup> Department of Materials Science and Engineering, Texas A&M University, College Station, TX 77843, USA

<sup>3</sup> Department of Industrial & Systems Engineering, Texas A&M University, College Station, TX 77843, USA

<sup>4</sup> Department of Engineering Technology & Industrial Distribution, Texas A&M University, College Station, TX 77843, USA

\* Correspondence: cma@tamu.edu

**Abstract:** Shell printing is an advantageous binder jetting technique that prints only a thin shell of the intended object to enclose the loose powder in the core. In this study, powder packing in the shell and core was investigated for the first time. By examining the density and microstructure of the printed samples, powder packing was found to be different between the shell and core. In addition, the powder particle size and layer thickness were found to affect the powder packing in the shell and core differently. At a 200  $\mu\text{m}$  layer thickness, for the 10  $\mu\text{m}$  and 20  $\mu\text{m}$  powders, the core was less dense than the shell and had a layered microstructure. At a 200  $\mu\text{m}$  layer thickness, for the 70  $\mu\text{m}$  powder, the core was denser and had a homogeneous microstructure. For the 20  $\mu\text{m}$  powder, by reducing the layer thickness from 200  $\mu\text{m}$  to 70  $\mu\text{m}$ , the core became denser than the shell, and the microstructure of the core became homogeneous. The different results could be attributed to the different scenarios of particle rearrangement between the shell and core for powders of different particle sizes and at different layer thicknesses. Considering that the core was denser and more homogeneous than the shell when the proper layer thickness and powder particle size were selected, shell printing could be a promising method to tailor density and reduce anisotropy.

**Keywords:** binder jetting; shell printing; powder packing



**Citation:** Miao, G.; Moghadasi, M.; Li, M.; Pei, Z.; Ma, C. Binder Jetting Additive Manufacturing: Powder Packing in Shell Printing. *J. Manuf. Mater. Process.* **2023**, *7*, 4. <https://doi.org/10.3390/jmmp7010004>

Academic Editor: Konda Gokuldoss Prashanth

Received: 5 December 2022

Revised: 20 December 2022

Accepted: 23 December 2022

Published: 27 December 2022



**Copyright:** © 2022 by the authors. Licensee MDPI, Basel, Switzerland. This article is an open access article distributed under the terms and conditions of the Creative Commons Attribution (CC BY) license (<https://creativecommons.org/licenses/by/4.0/>).

## 1. Introduction

Binder jetting is an additive manufacturing technique that makes parts from 3D data by selectively joining powder particles layer by layer using a liquid bonding agent [1]. Compared with other additive manufacturing techniques, binder jetting has some unique advantages, including the capability of processing various materials [2–9], no need for explicit support structure [9–12], and high scalability [13].

To print an object with binder jetting, binder is usually jetted to the whole cross-section of each layer. For example, to print the cube in Figure 1 through normal printing, binder is jetted to the whole square region. Shell printing is another way to print the cube. As shown in Figure 1, in shell printing, binder is only jetted to the region close to the surface to form a shell, and the core is left as a loose powder. The strength of the shell is high enough so that the movement of the loose powder in the core is restricted, and the green part can be depowdered and transported for sintering. After sintering, the powder in both the shell and core can be fused to form a solid cube.

Compared with normal printing, shell printing has several advantages. Firstly, less binder is needed for shell printing. Secondly, the debinding time is significantly reduced because only the thin shell contains binder. Lastly, the absence of binder in the core is beneficial for materials sensitive to binder residual.

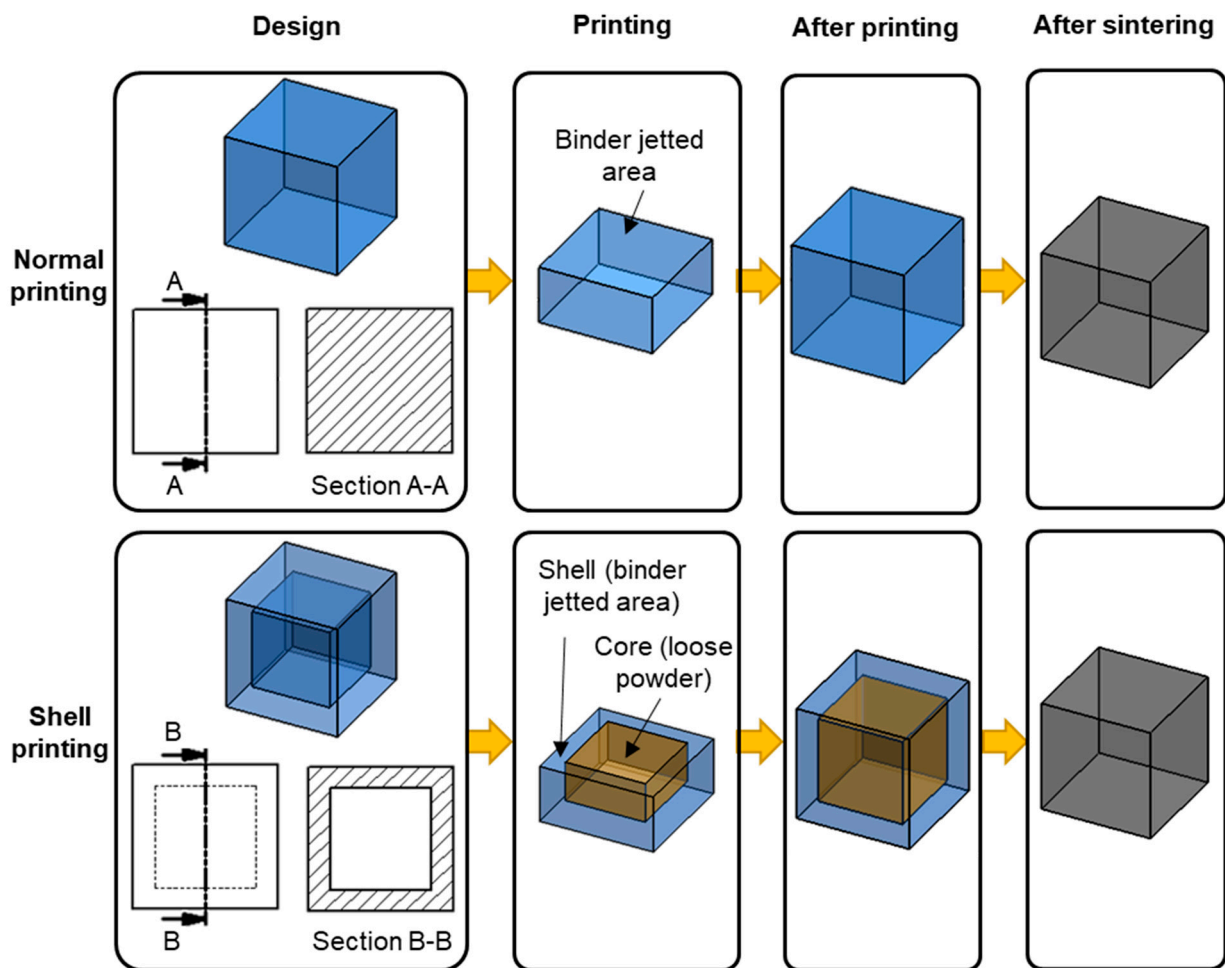


**Figure 1.** Schematic illustration of normal printing and shell printing.

Although shell printing has so many advantages, it is rarely reported. To the authors' best knowledge, there is only one reported study on shell printing in the literature: Frykholm et al. found that SS 316L samples printed through shell printing had higher strength than those printed through normal printing because the higher amount of carbon residual in the normally printed samples hindered the sintering process [14]. A subtle but important difference between the shell and core could lie in powder packing, which has never been reported in the literature. In this study, it is hypothesized that the powder packing density and structure are different between the shell and core. To test the hypothesis, alumina samples of different shell thicknesses were printed, and the powder packing density and the structure of the shell and core were examined. Alumina is selected because it does not chemically interact with the aqueous binder, and it allows debinding to occur in air to completely remove the binder. As a result, the observed powder packing density and structure, the focus of this study, were not chemically influenced by the binder, as seen in the reported study [14].

According to the literature, the powder particle size and layer thickness are two important process parameters that can affect powder packing in binder jetting [15–17]. To understand the effect of powder particle size and layer thickness on shell printing, powders of different particle sizes (10  $\mu\text{m}$ , 20  $\mu\text{m}$ , and 70  $\mu\text{m}$ ) were printed at different layer thicknesses (200  $\mu\text{m}$  and 70  $\mu\text{m}$ ), covering the most commonly used conditions in binder jetting.

## 2. Experimental Methods

### 2.1. Powder Characterization

Three alumina powders of different nominal particle sizes (10  $\mu\text{m}$ , 20  $\mu\text{m}$ , and 70  $\mu\text{m}$ ) were used in this study, as listed in Table 1. The three powders all had a spherical morphology. Scanning electron micrographs of the powders can be found elsewhere [18,19]. The particle size distribution of the three powders was measured using a laser diffraction particle size analyzer (Partica LA-960, Horiba, Japan). The measurements were conducted under dry conditions. The measurement results are plotted in Figure 2. According to the measurements, the three powders had D50 of about 10  $\mu\text{m}$ , 23  $\mu\text{m}$ , and 77  $\mu\text{m}$ , respectively, and D90 of about 17  $\mu\text{m}$ , 38  $\mu\text{m}$ , and 99  $\mu\text{m}$ , respectively.

**Table 1.** Different powders used in this study.

Nominal Particle Size ( $\mu\text{m}$ )	Supplier	Item Number
10	Denka	DAM-10
20	Denka	DAM20-S
70	Inframat Advanced Materials	26R8S70

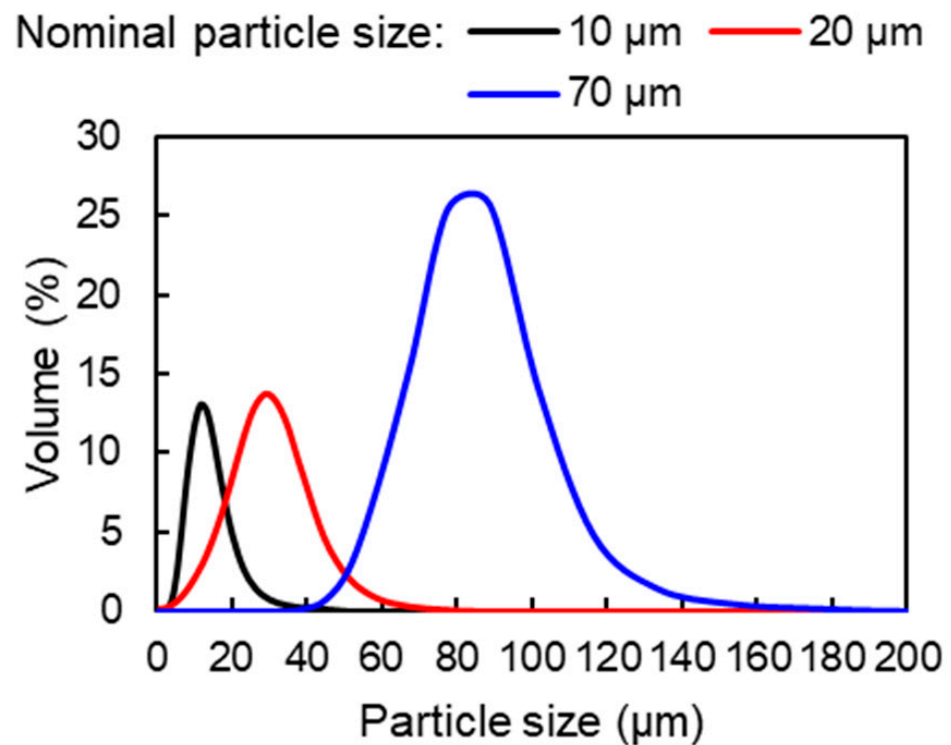


**Figure 2.** Particle size distribution of the three powders used in this study.

### 2.2. Printing with Powders of Different Particle Sizes

Printing experiments were carried out with three powders of different particle sizes. Each powder was used in three independent print jobs as replications. Therefore, a total of nine print jobs were conducted. Each print job included eight cubic samples, more specifically, two sets of four cubic samples of different designs. The designs are shown in Figure 3. All four designs had the same outside side length of 20 mm but different shell thicknesses and thus different shell volume fractions. The last design, with a shell thickness of 10 mm, had an effective shell volume fraction of 100%.

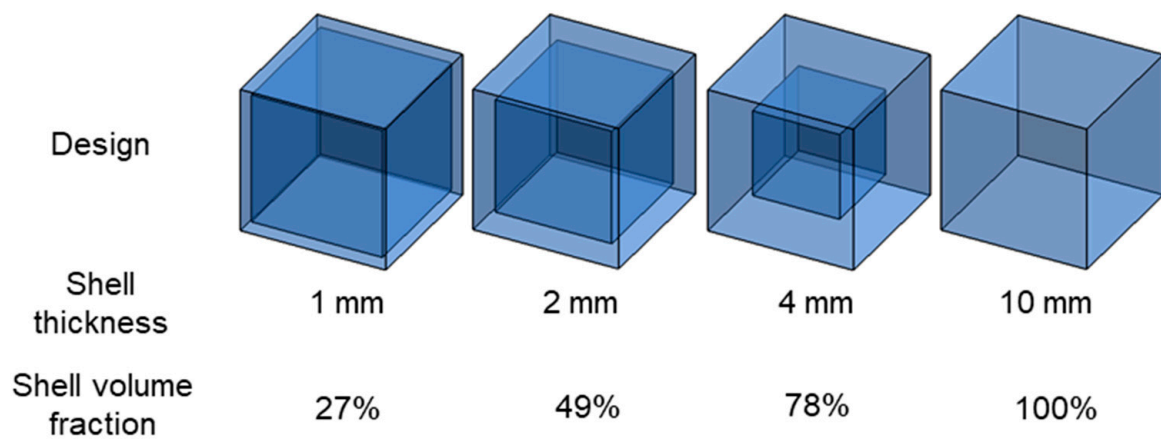


Figure 3. Designs for printing with powders of different particle sizes.

A commercially available binder jetting printer (Innovent+, ExOne Company, Huntingdon, PA, USA) was employed. The printing parameters were selected on the basis of the preliminary experiments and were kept the same for the three powders when possible (e.g., layer thickness was kept at 200  $\mu\text{m}$ ).

### 2.3. Printing at Different Layer Thicknesses

To study the effect of layer thickness on powder packing in shell printing, the 20  $\mu\text{m}$  powder was printed with two different layer thicknesses (i.e., 70  $\mu\text{m}$  and 200  $\mu\text{m}$ ). Samples of different heights were printed at the different layer thicknesses to keep the number of powder layers similar. The designs shown in Figure 3 were printed at the 200  $\mu\text{m}$  layer thickness, while the designs shown in Figure 4 were printed at the 70  $\mu\text{m}$  layer thickness. All the printing parameters except layer thickness were kept the same. The four designs, with two replications of each design, were printed together with a random layout in the same print job. Each print job was replicated three times.

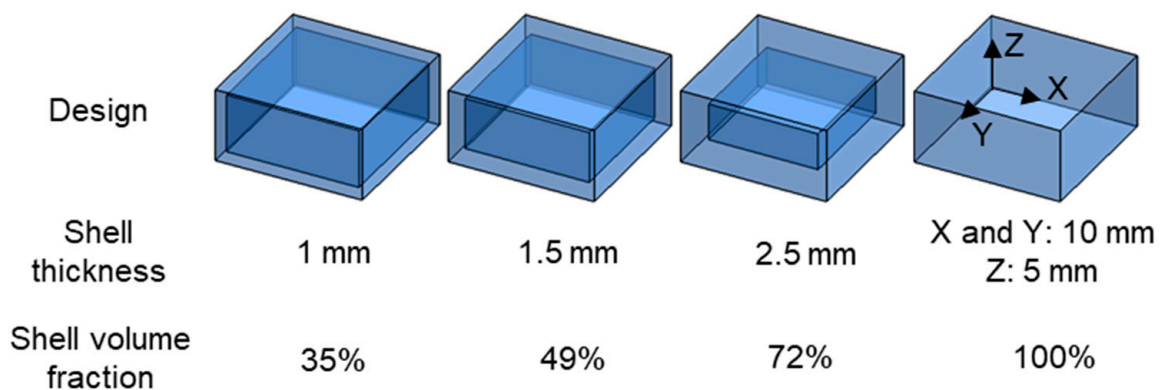


Figure 4. Designs printed at the reduced layer thickness.

### 2.4. Post-Processing

The printed samples were cured in air in a furnace (DX402C, Yamato Scientific America, Santa Clara, CA, USA) at 200  $^{\circ}\text{C}$  for 240 min. Then, the cured samples were transported to another furnace (KSL-1700X, MTI, USA) for debinding and sintering. The debinding was conducted by heating the samples to 480  $^{\circ}\text{C}$  in air and holding for 220 min, and the sintering was conducted by heating the samples to 1700  $^{\circ}\text{C}$  in air and holding for 120 min.

### 2.5. Density Measurement

The density of the green samples (i.e., cured samples) was measured using the geometric method. The dimensions of the green samples were measured using a caliper with a

resolution of 0.01 mm. The mass of the green samples was measured using a scale with a resolution of 0.001 g. Given the dimensions and mass of the green samples, the green density was calculated.

The brown density of the samples was estimated by dividing the mass of the samples after debinding by the volume of the samples before debinding. The volume of the samples before debinding was used because the brown samples were too weak to determine the volume.

The density of the sintered samples was measured using the Archimedes method following the ISO-18754 standard [20].

The measured green, brown, and sintered densities were divided by the theoretical density of alumina (i.e., 3.97 g/cm<sup>3</sup>) to calculate the relative densities. The relative densities were used for all the analyses in this study.

### 2.6. Microstructure Characterization

An X-ray computed tomography (CT) system (X50, NSI, Rogers, MN, USA) was used to characterize the microstructure of the green and sintered samples. Fast Fourier transform (FFT) was used to process CT images.

The microstructure of the sintered samples was also characterized with a scanning electron microscope (SEM). Before the SEM characterization, the sintered samples were sectioned, ground, and coated with platinum using a sputter coater (108 Auto, Cressington, Watford, UK).

## 3. Results

### 3.1. The Effect of Powder Particle Size on Powder Packing in Shell Printing

The green density of the samples printed with the 10 μm, 20 μm, and 70 μm powders is plotted as a function of shell volume fraction in Figure 5a. For the 10 μm powder, green density slightly increased as shell volume fraction increased. Similarly, green density slightly increased with increasing shell volume fraction for the 20 μm powder, but the increase was smaller than that of the 10 μm powder. Different from the 10 μm and 20 μm powders, green density significantly decreased with increasing shell volume fraction for the 70 μm powder. Figure 5b shows the brown density of the samples printed with the three powders. The difference between brown and green densities for the same type of samples was less than or around 1%. The trends observed for green density held for brown density as well.

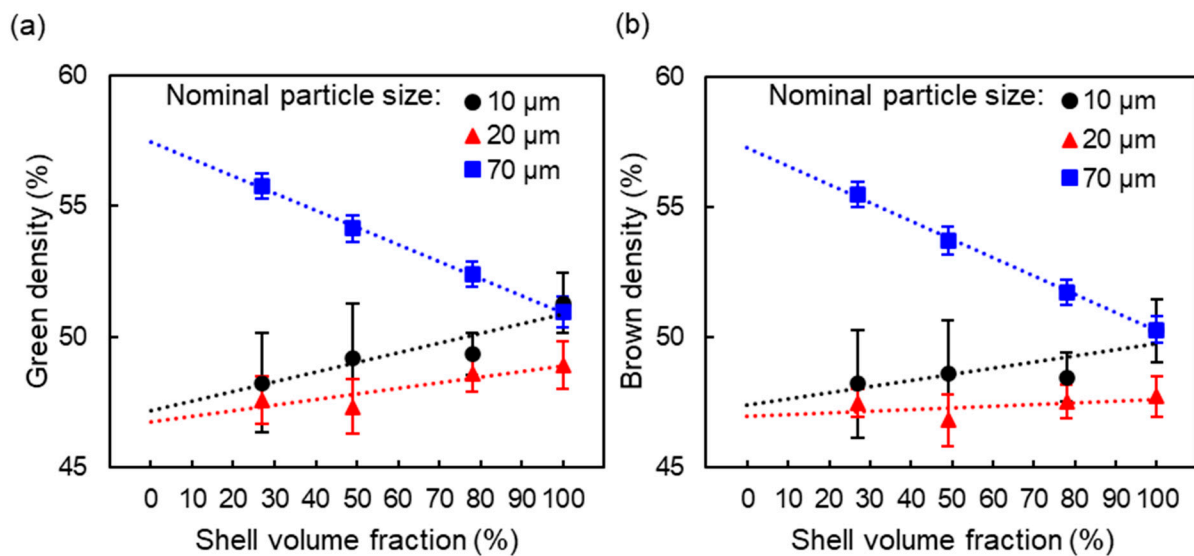
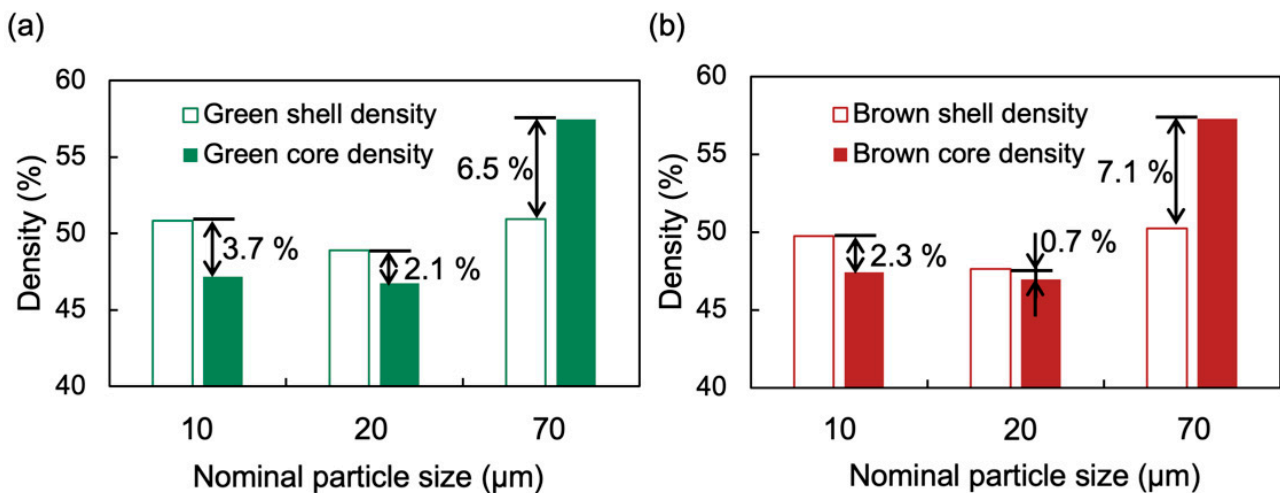


Figure 5. Densities of samples printed with powders of different particle sizes: (a) green density and (b) brown density.

According to Figure 5, the shell and core of the samples had different densities, so the overall density changed with shell volume fraction. The overall density ( $\rho$ ) of any sample can be expressed with the shell density ( $\rho_S$ ), core density ( $\rho_C$ ), and shell volume fraction ( $f_S$ ):

$$\rho = \rho_S f_S + \rho_C (1 - f_S) \quad (1)$$

To find out the shell and core densities of the samples printed with each powder, Equation (1) was fitted to the data points of each powder in Figure 5. The estimated shell and core densities in both the green and brown states are plotted in Figure 6. As shown in Figure 6, the shell density was higher than the core density for the green and brown samples printed with the 10  $\mu\text{m}$  and 20  $\mu\text{m}$  powders. For the samples printed with the 70  $\mu\text{m}$  powder, the core density was higher than the shell density. These results agree well with a recent study on the difference between powder bed and green density using the same powder [21]. In addition, from the green state to the brown state, the density difference between the shell and the core decreased for the 10  $\mu\text{m}$  and 20  $\mu\text{m}$  powders (from 3.7% to 2.3% for the 10  $\mu\text{m}$  powder and from 2.1% to 0.7% for the 20  $\mu\text{m}$  powder) but increased for the 70  $\mu\text{m}$  powder (from 6.5% to 7.1%). The change in the density difference was related to the debinding-induced decrease of the shell density. Because the binder in the shell was burned out through debinding, the density of the shell decreased after debinding. Because there was no binder in the core, the density of the core was unchanged after debinding.



**Figure 6.** Estimated shell and core densities of the samples printed with powders of different particle sizes: (a) green density and (b) brown density.

The microstructures of the green samples printed with the three powders are compared in Figure 7. The shell and core could be easily differentiated in all three samples. For samples printed with the 10  $\mu\text{m}$  and 20  $\mu\text{m}$  powders, the powder layers were evident in both the shell and the core. For the sample printed with the 70  $\mu\text{m}$  powder, the layered microstructure was not visually identifiable, especially in the core.

To identify the patterns of the features in the CT images, FFT was used to process the CT images of the shell and core, which are marked with red squares in Figure 7. The spatial frequency spectrum along the Z direction is plotted in Figure 8. For the samples printed with the 10  $\mu\text{m}$  and 20  $\mu\text{m}$  powders, peaks were found for both the shell and core at a spatial frequency of 5 cycles/mm, whose inverse matches the layer thickness (i.e., 200  $\mu\text{m}$ ). For the sample printed with the 70  $\mu\text{m}$  powder, although the powder layers are not easily identifiable in Figure 7, a peak was also found at the frequency corresponding to the layer thickness for the shell. However, no such peak stood out for the core. This indicates that the core was more homogeneous than the shell.

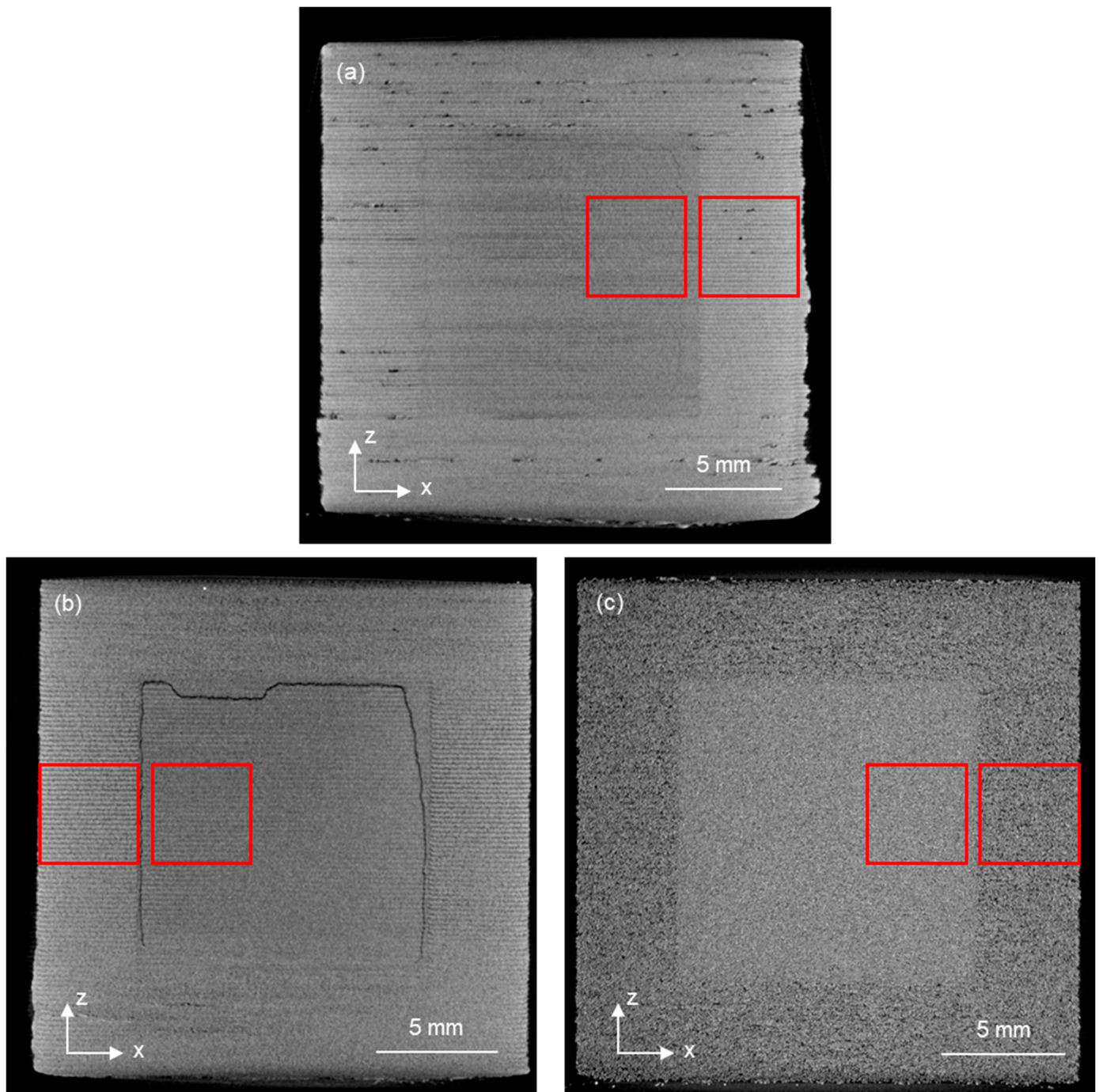


**Figure 7.** CT images of the green samples printed with powders of different particle sizes: (a) 10  $\mu\text{m}$ , (b) 20  $\mu\text{m}$ , and (c) 70  $\mu\text{m}$ .

### 3.2. The Effect of Layer Thickness on Powder Packing in Shell Printing

Figure 9 shows the green, brown, and sintered densities of the samples printed at the 70  $\mu\text{m}$  and 200  $\mu\text{m}$  layer thicknesses with the 20  $\mu\text{m}$  powder. Different trends were observed at different layer thicknesses. At the 200  $\mu\text{m}$  layer thickness, all three densities increased with increasing shell volume fractions. The increasing trend became less significant when the samples underwent debinding or sintering. At the 70  $\mu\text{m}$  layer thickness, all densities decreased with increasing shell volume fraction.

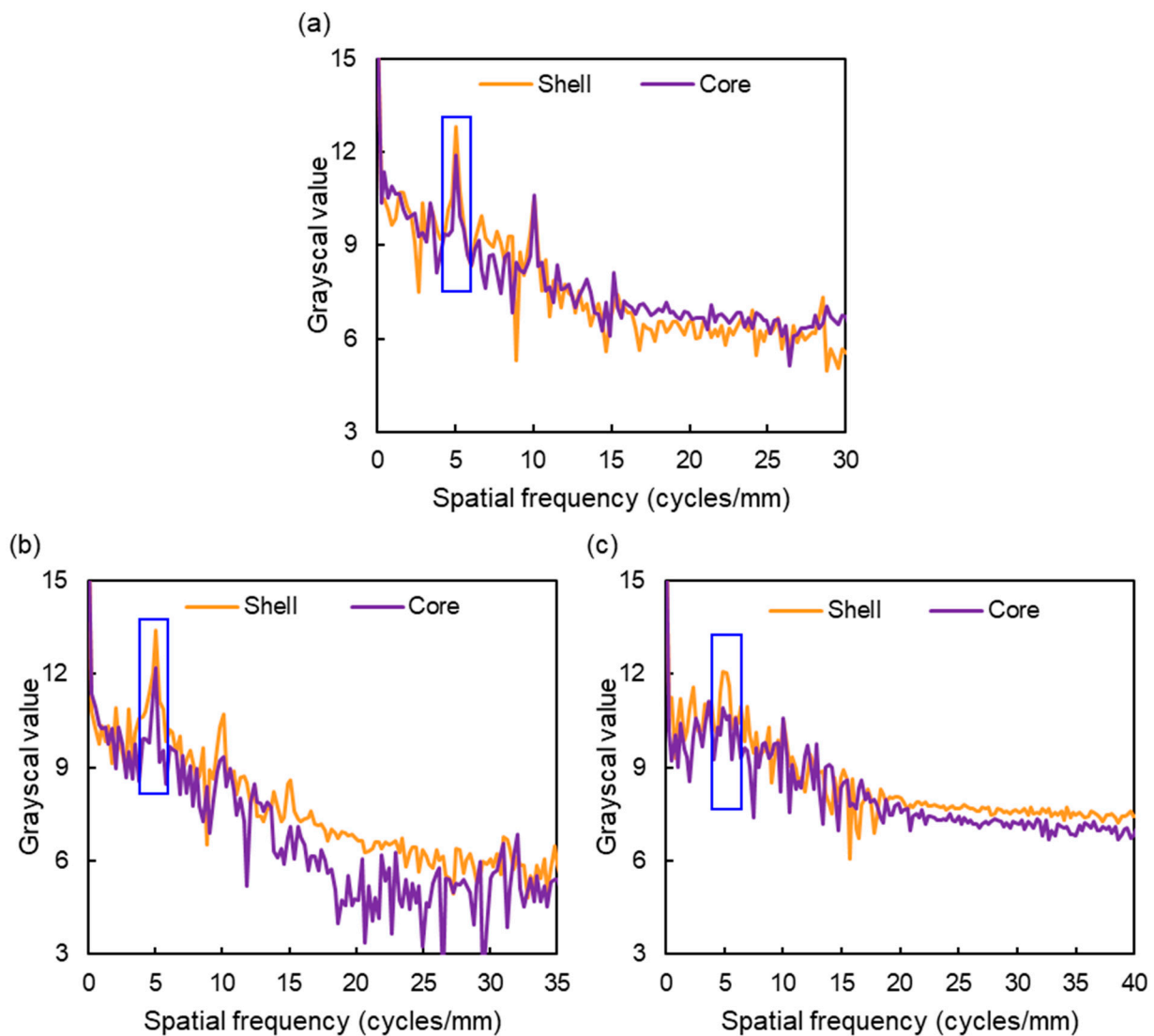


**Figure 8.** Spatial frequency spectra of the shell and core of the samples printed with powders of different particle sizes: (a) 10  $\mu\text{m}$ , (b) 20  $\mu\text{m}$ , and (c) 70  $\mu\text{m}$ .

Regression analysis was performed using the data points in Figure 9 according to Equation (1) to estimate the shell and core densities of the green, brown, and sintered samples printed at the 70  $\mu\text{m}$  and 200  $\mu\text{m}$  layer thicknesses with the 20  $\mu\text{m}$  powder. The estimated shell and core densities of the samples are plotted in Figure 10. The core had a higher density at the low layer thickness, while the shell had a higher density at the high thickness. The density difference between the shell and the core is also plotted in Figure 10. From the green state to the brown state, the density difference between the shell and the core increased at the 70  $\mu\text{m}$  layer thickness (from 1.5% to 2.6%) but decreases at the 200  $\mu\text{m}$  layer thickness (from 2.1% to 0.7%). This change in Figure 10 is similar to that in Figure 6. The reason is the mass loss during debinding. From the brown state to the sintered state, the density difference between the shell and core increased at the 70  $\mu\text{m}$  layer thickness (from 2.6% to 3.2%) but decreased at the 200  $\mu\text{m}$  layer thickness (from 0.7% to 0.2%). The reason for this change was probably that the binder in the shell created pores when burned out, hindering the densification of the shell.



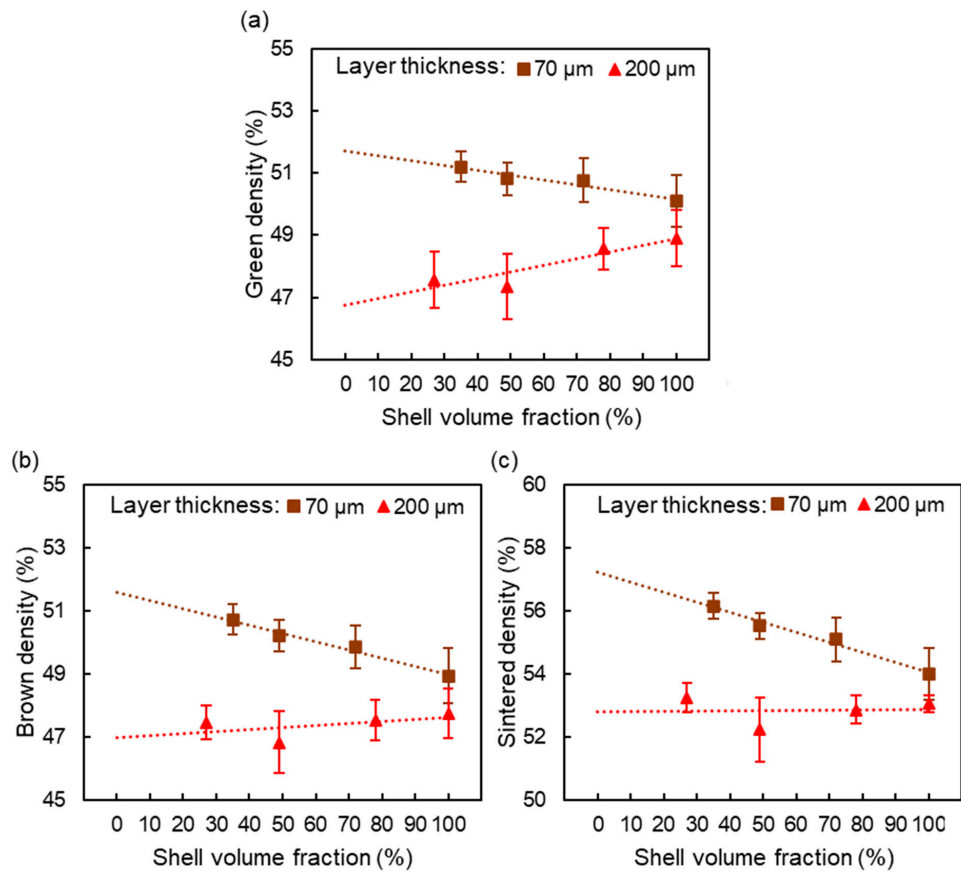


**Figure 9.** Densities of samples printed at different layer thicknesses: (a) green density, (b) brown density, and (c) sintered density.

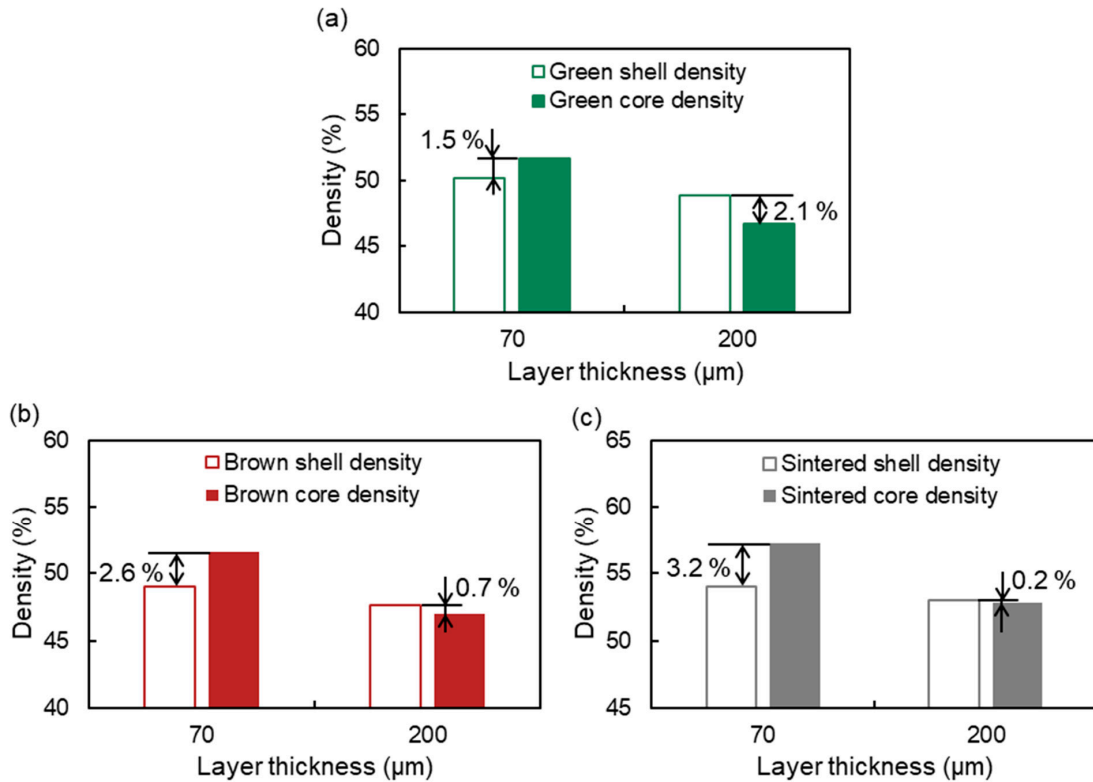


**Figure 10.** Estimated shell and core densities of the samples printed at different layer thicknesses: (a) green density, (b) brown density, and (c) sintered density.

The microstructure of the green sample printed at the 70  $\mu\text{m}$  layer thickness is compared with that at the 200  $\mu\text{m}$  layer thickness in Figure 11. At the 70  $\mu\text{m}$  layer thickness, no layered microstructure was observed for either the shell or core. At the 200  $\mu\text{m}$  layer thickness, a layered microstructure was present for both the shell and core.

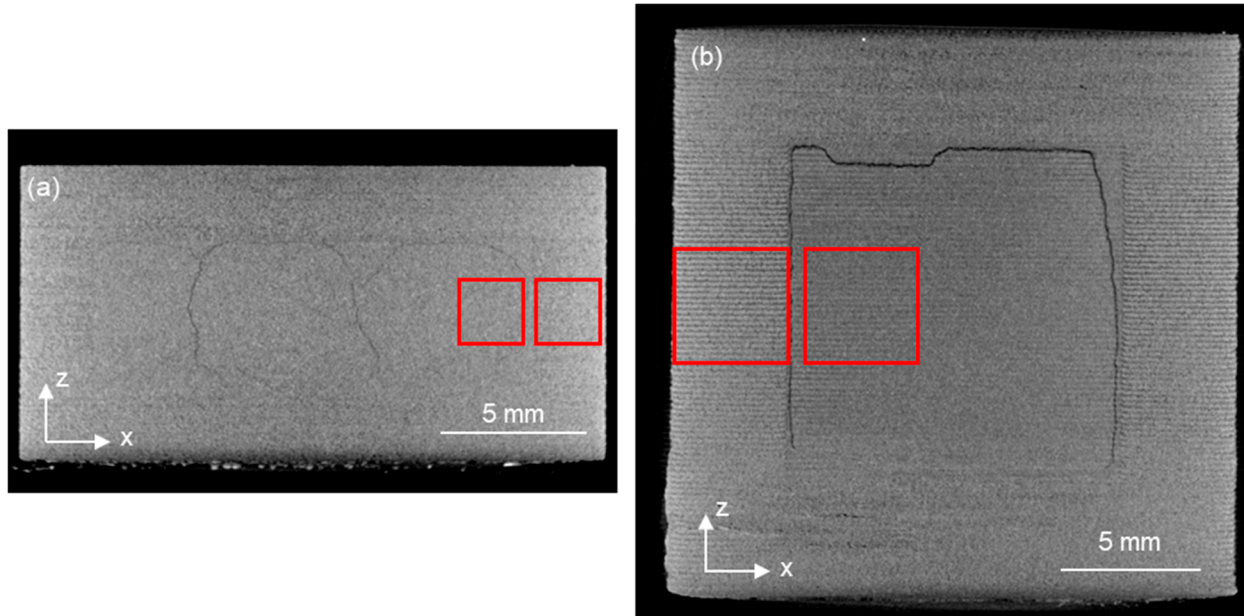


**Figure 11.** CT images of the green samples printed with the 20  $\mu\text{m}$  powder at different layer thicknesses: (a) 70  $\mu\text{m}$  and (b) 200  $\mu\text{m}$ .

The square regions in the CT image of the shell and core of the sample printed at the 70  $\mu\text{m}$  layer thickness (Figure 11a) were processed with FFT. The spatial frequency spectrum along the Z axis is compared with that at the 200  $\mu\text{m}$  layer thickness in Figure 12. No peak was observed at the frequency corresponding to the layer thickness (circled with the blue box) for either the shell or core of the sample printed at the 70  $\mu\text{m}$  layer thickness. A possible reason is that the layer thickness was close to the resolution of the CT ( $\sim 25 \mu\text{m}$ ), especially considering the lack of a peak even in the shell. For the sample printed at the 200  $\mu\text{m}$  layer thickness, peaks were found for both the shell and the core at the frequency corresponding to the layer thickness.

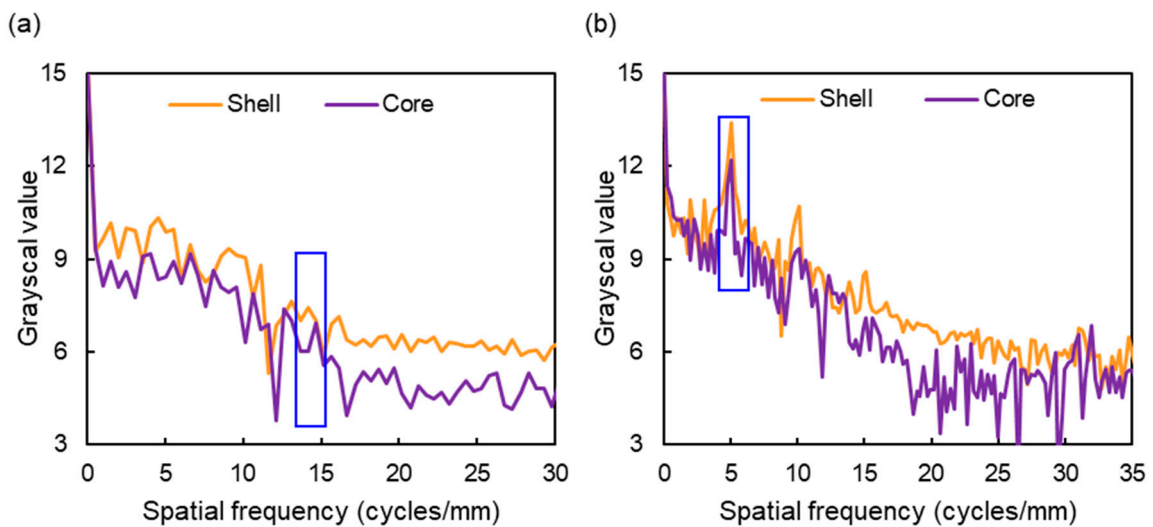


**Figure 12.** Spatial frequency spectra of the shell and core of the samples printed with 20  $\mu\text{m}$  powder at different layer thicknesses: (a) 70  $\mu\text{m}$  and (b) 200  $\mu\text{m}$ .

The microstructures of the sintered samples printed at the 70  $\mu\text{m}$  and 200  $\mu\text{m}$  layer thicknesses with the 20  $\mu\text{m}$  powder are shown in Figure 13. For the sample printed at the 70  $\mu\text{m}$  layer thickness, according to the SEM image, the shell had a layered structure, and the core was homogeneous. For the sample printed at the 200  $\mu\text{m}$  layer thickness, the layered structure was evident in the shell but was less noticeable in the core.

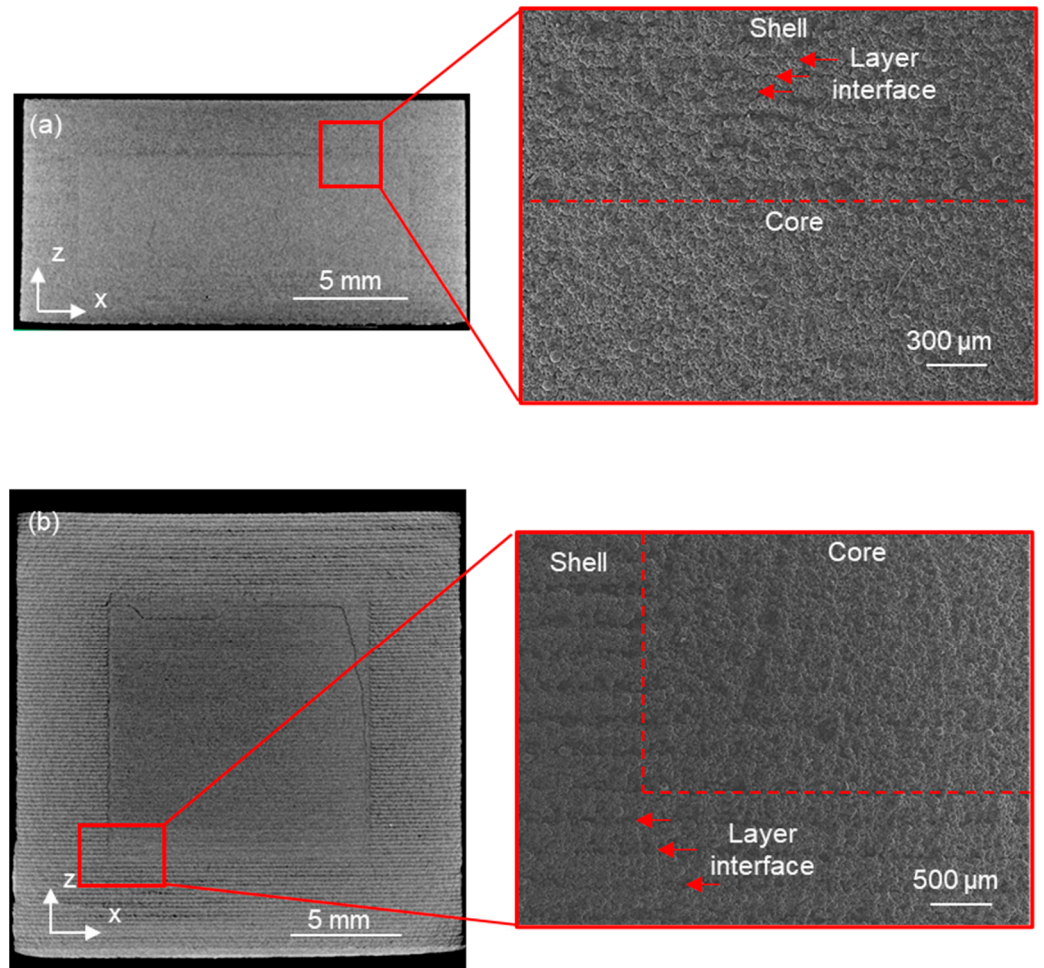


**Figure 13.** CT and SEM images of the sintered samples printed with the 20  $\mu\text{m}$  powder at different layer thicknesses: (a) 70  $\mu\text{m}$  and (b) 200  $\mu\text{m}$ .

#### 4. Discussion of Powder Packing

Table 2 summarizes the results of core density (compared with shell density) and core microstructure (layered or homogeneous). These results show a strong dependence on the ratio of layer thickness to powder particle size. The different results are likely related to the different particle rearrangement scenarios illustrated in Figure 14: spreading-induced rearrangement and binder-induced rearrangement.

**Table 2.** Summary of the printing results.

Powder Particle Size ( $\mu\text{m}$ )	Layer Thickness ( $\mu\text{m}$ )	Ratio of Layer Thickness to Powder Particle Size	Core Density Compared with Shell Density	Core Microstructure
10	200	20	Lower	Layered
20	200	10	Lower	Layered
70	200	2.9	Higher	Homogeneous
20	70	3.5	Higher	Homogeneous

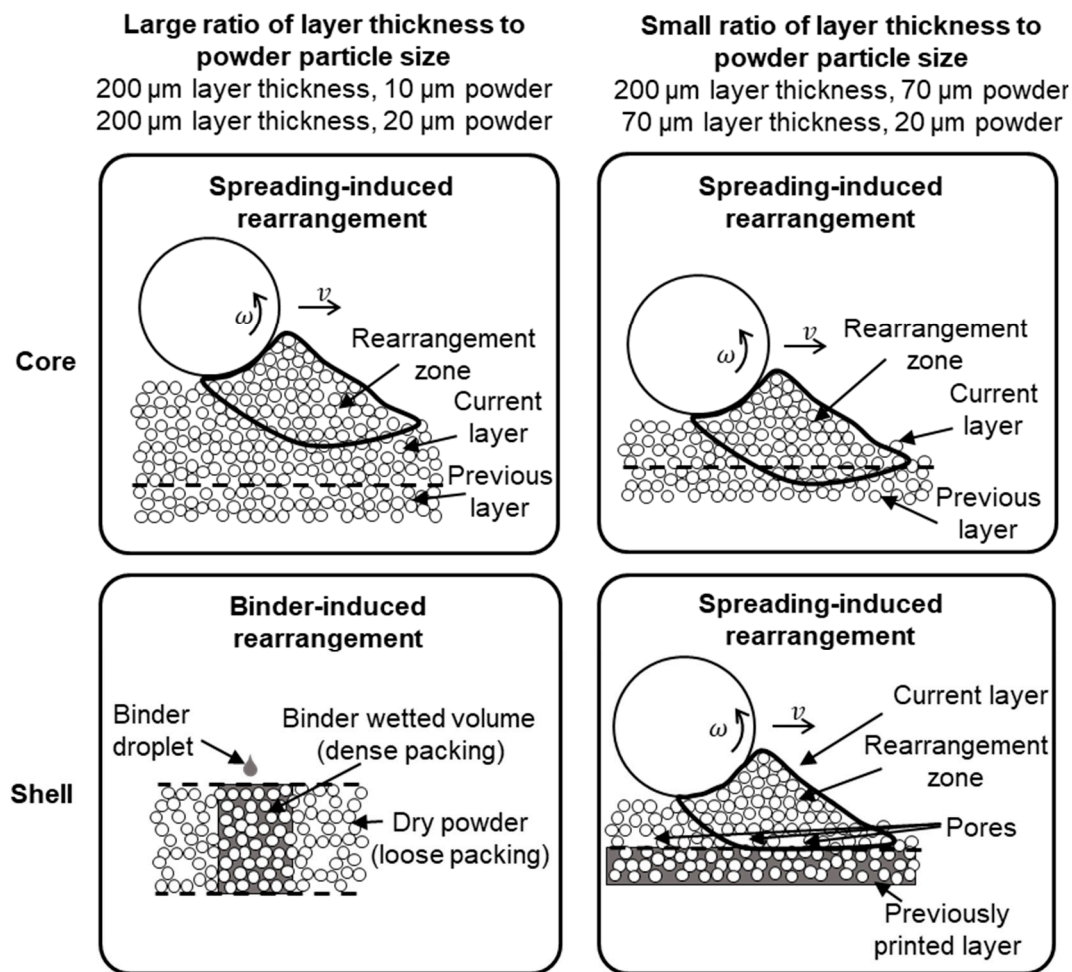


**Figure 14.** Schematic illustration of different particle rearrangement scenarios under different printing conditions ( $\omega$  is the roller rotation speed while  $v$  is the roller traverse speed).

In the samples printed with the 10 μm and 20 μm powders at the 200 μm layer thickness (i.e., at a large ratio of layer thickness to powder particle size), the shell was found to be denser than the core, and a layered microstructure was observed in the core. The higher density of the shell compared with that of the core was probably caused by the binder-induced rearrangement shown in Figure 14. Because of the capillary bridging effect of the binder, the binder–powder interaction could slightly rearrange powder particles and improve the powder packing density [22,23]. The reason for the layered microstructure in the core was probably that the powder packing at the bottom of the powder layer was different from that at the top of the powder layer. According to the literature, a counter-rotating roller can efficiently rearrange powder particles to achieve a high powder bed density [24–27]. However, there must be a limit for particle rearrangement zone. Beyond the limit (e.g., outside of the rearrangement zone shown in Figure 14), the roller could not rearrange the particles anymore. Because the ratio of layer thickness to powder particle size was large, the rearrangement zone probably covered only the top part of the powder layer, and thus, the top part could have a different density from the bottom part.

For the samples printed with the 70 μm powder at the 200 μm layer thickness and those printed with the 20 μm powder at the 70 μm layer thickness (i.e., at a small ratio of layer thickness to powder particle size), the core was found to have a higher density than the shell and a homogenous (unlayered) microstructure. These results of density and microstructure are believed to be related to each other and caused by more voids in the shell than the core, especially at the interface of powder layers. For the shell, because the previously printed layer restricted the movement of the powder particles in the current

layer [5], voids could occur at the interface of powder layers, as shown in Figure 14. However, for the core, the voids at the interface of powder layers could be avoided through spreading-induced rearrangement. As shown in Figure 14, when the ratio of layer thickness to powder particle size was small, the rearrangement zone covered both the whole current layer and the previous layer. This way, the powder particles from both layers were mixed, and the voids at the interface of the powder layers could be avoided.

Because of the high density and homogeneous microstructure of the core at a small ratio of layer thickness to powder particle size, shell printing could be used for applications that require a high density or a high degree of isotropy. In addition to density and microstructure control, shell printing has intrinsic advantages, such as lower binder usage, short debinding time, and less binder residual. Furthermore, shell printing is compatible with other methods for density and microstructure control, such as powder granulation [16,28–30], mixing powders of different sizes [17,31], powder bed compaction [32], and infiltration [33–35]. It is possible to combine shell printing with these methods.

## 5. Conclusions

Powder packing in shell printing was investigated for the first time. Cubes of different shell thicknesses were printed with powders of different particle sizes and at different layer thicknesses. For fine powders (i.e., the 10  $\mu\text{m}$  and 20  $\mu\text{m}$  powders), when printed at the large layer thickness (i.e., 200  $\mu\text{m}$ ), a layered microstructure was observed in both the shell and the core, and the shell density was higher than the core density. For coarse powder (i.e., the 70  $\mu\text{m}$  powder), when printed at the same layer thickness (i.e., 200  $\mu\text{m}$ ), the core was denser and more homogeneous than the shell. For the 20  $\mu\text{m}$  powder, the core became denser than the shell, and the microstructure of the core became homogeneous by reducing the layer thickness from 200  $\mu\text{m}$  to 70  $\mu\text{m}$ . The different densities and microstructures of the shell and the core could be explained by the different scenarios of particle rearrangement for powders of different particle sizes and at different layer thicknesses. This new knowledge can help researchers better understand the unique powder packing behaviors in shell printing. It also indicates that shell printing, or selective printing, could be a useful method to tailor density and microstructure.

**Author Contributions:** Conceptualization, C.M.; Data curation, G.M., M.M. and M.L.; Formal analysis, G.M.; Funding acquisition, C.M. and Z.P.; Investigation, G.M.; Methodology, G.M., C.M., M.M. and M.L.; Project administration, C.M. and Z.P.; Resources, C.M. and Z.P.; Supervision, C.M. and Z.P.; Validation, G.M.; Visualization, G.M. and C.M.; Writing—original draft, G.M.; Writing—review and editing, G.M. and C.M. All authors have read and agreed to the published version of the manuscript.

**Funding:** This material was based on work supported by the National Science Foundation under Grant No. 1762341.

**Institutional Review Board Statement:** Not applicable.

**Informed Consent Statement:** Not applicable.

**Data Availability Statement:** Not applicable.

**Acknowledgments:** The authors would like to acknowledge Denka for providing the powders.

**Conflicts of Interest:** The authors have no relevant financial or non-financial interest to disclose.

## References

1. ISO/ASTM 52900:2021; Standard Terminology for Additive Manufacturing-General Principles-Terminology. ASTM International: West Conshohocken, PA, USA, 2021.
2. Du, W.; Ren, X.; Pei, Z.; Ma, C. Ceramic Binder Jetting Additive Manufacturing: A Literature Review on Density. *J. Manuf. Sci. Eng.* **2020**, *142*, 040801. [[CrossRef](#)]
3. Li, M.; Du, W.; Elwany, A.; Pei, Z.; Ma, C. Metal Binder Jetting Additive Manufacturing: A Literature Review. *J. Manuf. Sci. Eng.* **2020**, *142*, 090801. [[CrossRef](#)]

4. Mostafaei, A.; Elliott, A.; Barnes, J.; Cramer, C.; Nandwana, P.; Chmielus, M. Binder Jet 3D Printing—Process Parameters, Materials, Properties, and Challenges. *Prog. Mater. Sci.* **2021**, *119*, 100707. [[CrossRef](#)]
5. Ziaee, M.; Crane, N. Binder Jetting: A Review of Process, Materials, and Methods. *Addit. Manuf.* **2019**, *28*, 781–801. [[CrossRef](#)]
6. Chavez, L.; Ibañez, P.; Wilburn, B.; Alexander, D.; Stewart, C.; Wicker, R.; Lin, Y. The Influence of Printing Parameters, Post-Processing, and Testing Conditions on the Properties of Binder Jetting Additive Manufactured Functional Ceramics. *Ceramics* **2020**, *3*, 65–77. [[CrossRef](#)]
7. Sachs, E.; Cima, M.; Cornie, J.; Brancazio, D.; Brecht, J.; Curodeau, A.; Fan, T.; Khanuja, S.; Lauder, A.; Lee, J. Three-Dimensional Printing: The Physics and Implications of Additive Manufacturing. *CIRP Ann.* **1993**, *42*, 257–260. [[CrossRef](#)]
8. Bourell, D.; Kruth, J.; Leu, M.; Levy, G.; Rosen, D.; Beese, A.; Clare, A. Materials for Additive Manufacturing. *CIRP Ann.* **2017**, *66*, 659–681. [[CrossRef](#)]
9. Guo, N.; Leu, M. Additive Manufacturing: Technology, Applications and Research Needs. *Front. Mech. Eng.* **2013**, *8*, 215–243. [[CrossRef](#)]
10. Seitz, H.; Rieder, W.; Irsen, S.; Leukers, B.; Tille, C. Three-Dimensional Printing of Porous Ceramic Scaffolds for Bone Tissue Engineering. *J. Biomed. Mater. Res. Part B* **2005**, *74*, 782–788. [[CrossRef](#)]
11. Williams, C.; Cochran, J.; Rosen, D. Additive Manufacturing of Metallic Cellular Materials via Three-Dimensional Printing. *Int. J. Adv. Manuf. Technol.* **2011**, *53*, 231–239. [[CrossRef](#)]
12. Graybill, B.; Li, M.; Malawey, D.; Ma, C.; Alvarado-Orozco, J.-M.; Martinez-Franco, E. Additive Manufacturing of Nickel-Based Superalloys. In Proceedings of the ASME International Manufacturing Science and Engineering Conference, College Station, TX, USA, 18–22 June 2018.
13. Zocca, A.; Lima, P.; Günster, J. LSD-Based 3D Printing of Alumina Ceramics. *J. Ceram. Sci. Technol.* **2017**, *8*, 141–148.
14. Frykholm, R.; Takeda, Y.; Andersson, B.; Carlström, R. Solid State Sintered 3-D printing Component by Using Inkjet (Binder) Method. *J. Jpn. Soc. Powder Powder Metall.* **2016**, *63*, 421–426. [[CrossRef](#)]
15. Miao, G.; Du, W.; Pei, Z.; Ma, C. A Literature Review on Powder Spreading in Additive Manufacturing. *Addit. Manuf.* **2022**, *58*, 103029. [[CrossRef](#)]
16. Miao, G.; Du, W.; Moghadasi, M.; Pei, Z.; Ma, C. Ceramic Binder Jetting Additive Manufacturing: Effects of Granulation on Properties of Feedstock Powder and Printed and Sintered Parts. *Addit. Manuf.* **2020**, *36*, 101542. [[CrossRef](#)]
17. Du, W.; Roa, J.; Hong, J.; Liu, Y.; Pei, Z.; Ma, C. Binder Jetting Additive Manufacturing: Effect of Particle Size Distribution on Density. *J. Manuf. Sci. Eng.* **2021**, *143*, 091002. [[CrossRef](#)]
18. Li, M.; Miao, G.; Moghadasi, M.; Pei, Z.; Ma, C. Ceramic Binder Jetting Additive Manufacturing: Relationships Among Powder Properties, Feed Region Density, and Powder Bed Density. *Ceram. Int.* **2021**, *47*, 25147–25151. [[CrossRef](#)]
19. Mariani, M.; Beltrami, R.; Brusa, P.; Galassi, C.; Ardito, R.; Lecis, N. 3D Printing of Fine Alumina Powders by Binder Jetting. *J. Eur. Ceram. Soc.* **2021**, *41*, 5307–5315. [[CrossRef](#)]
20. ISO 18754:2020; Fine Ceramics (Advanced Ceramics, Advanced Technical Ceramics)—Determination of Density and Apparent Porosity. International Organization for Standardization: Vernier, Geneva, Switzerland, 2020.
21. Li, M.; Miao, G.; Du, W.; Pei, Z.; Ma, C. Difference between Powder Bed Density and Green Density for a Free-Flowing Powder in Binder Jetting Additive Manufacturing. *J. Manuf. Process.* **2022**, *84*, 448–456. [[CrossRef](#)]
22. Bai, Y.; Wall, C.; Pham, H.; Esker, A.; Williams, C. Characterizing Binder–Powder Interaction in Binder Jetting Additive Manufacturing via Sessile Drop Goniometry. *J. Manuf. Sci. Eng.* **2019**, *141*, 011005. [[CrossRef](#)]
23. Cima, M.; Lauder, A.; Khanuja, S.; Sachs, E. *Microstructural Elements of Components Derived from 3D Printing*; International Solid Freeform Fabrication Symposium: Austin, TX, USA, 1992.
24. Haeri, S.; Wang, Y.; Ghita, O.; Sun, J. Discrete Element Simulation and Experimental Study of Powder Spreading Process in Additive Manufacturing. *Powder Technol.* **2017**, *306*, 45–54. [[CrossRef](#)]
25. Zhang, J.; Tan, Y.; Bao, T.; Xu, Y.; Xiao, X.; Jiang, S. Discrete Element Simulation of the Effect of Roller-Spreading Parameters on Powder-Bed Density in Additive Manufacturing. *Materials* **2020**, *13*, 2285. [[CrossRef](#)] [[PubMed](#)]
26. Budding, A.; Vaneker, T. New Strategies for Powder Compaction in Powder-Based Rapid Prototyping Techniques. *Procedia CIRP* **2013**, *6*, 527–532. [[CrossRef](#)]
27. Nan, W.; Pasha, M.; Ghadiri, M. Numerical Simulation of Particle Flow and Segregation During Roller Spreading Process in Additive Manufacturing. *Powder Technol.* **2020**, *364*, 811–821. [[CrossRef](#)]
28. Du, W.; Miao, G.; Pei, Z.; Ma, C. Comparison of Flowability and Sinterability among Different Binder Jetting Feedstock Powders: Granulated Powder, Micropowder, and Nanopowder. *J. Micro Nano-Manuf.* **2021**, *9*, 021008. [[CrossRef](#)]
29. Du, W.; Miao, G.; Liu, L.; Ma, C.; Pei, Z. Binder Jetting Additive Manufacturing of Ceramics: Feedstock Powder Preparation by Spray Freeze Granulation. In Proceedings of the ASME International Manufacturing Science and Engineering Conference, Erie, PA, USA, 10–14 June 2019.
30. Du, W.; Miao, G.; Liu, L.; Ma, C.; Pei, Z. Binder Jetting Additive Manufacturing of Ceramics: Comparison of Flowability and Sinterability between Raw and Granulated Powders. In Proceedings of the ASME International Manufacturing Science and Engineering Conference, Erie, PA, USA, 10–14 June 2019.
31. Du, W.; Ren, X.; Chen, Y.; Ma, C.; Radovic, M.; Pei, Z. Model Guided Mixing of Ceramic Powders with Graded Particle Sizes in Binder Jetting Additive Manufacturing. In Proceedings of the ASME International Manufacturing Science and Engineering Conference, College Station, TX, USA, 18–22 June 2018.

32. Moghadasi, M.; Miao, G.; Li, M.; Pei, Z.; Ma, C. Combining Powder Bed Compaction and Nanopowder to Improve Density in Ceramic Binder Jetting Additive Manufacturing. *Ceram. Int.* **2021**, *47*, 35348–35355. [[CrossRef](#)]
33. Porter, Q.; Pei, Z.; Ma, C. Binder Jetting and Infiltration of Metal Matrix Nanocomposites. *J. Manuf. Sci. Eng.* **2022**, *144*, 074502. [[CrossRef](#)]
34. Yin, X.; Travitzky, N.; Melcher, R.; Greil, P. Three-dimensional Printing of  $\text{TiAl}_3/\text{Al}_2\text{O}_3$  Composites. *Int. J. Mater. Res.* **2006**, *97*, 492–498. [[CrossRef](#)]
35. Maleksaeedi, S.; Eng, H.; Wiria, F.; Ha, T.; He, Z. Property Enhancement of 3D-Printed Alumina Ceramics Using Vacuum Infiltration. *J. Mater. Process. Technol.* **2014**, *214*, 1301–1306. [[CrossRef](#)]

**Disclaimer/Publisher's Note:** The statements, opinions and data contained in all publications are solely those of the individual author(s) and contributor(s) and not of MDPI and/or the editor(s). MDPI and/or the editor(s) disclaim responsibility for any injury to people or property resulting from any ideas, methods, instructions or products referred to in the content.